



Hierarchically porous ceramics via direct writing of preceramic polymer-triblock copolymer inks

John J. Bowen ^{1,2}, Shahryar Mooraj ³, Jacob A. Goodman ⁴, Siyuan Peng ³, Dayton P. Street ^{1,6}, Benito Roman-Manso ⁷, Emily C. Davidson ⁷, Kara L. Martin ^{1,2}, Lisa M. Rueschhoff ¹, Scott N. Schiffres ^{4,5}, Wen Chen ^{3,*}, Jennifer A. Lewis ^{7,8,*}, Matthew B. Dickerson ^{1,*}

Hierarchically porous ceramics possess tailored porosity across multiple length scales, giving rise to materials with low density, high specific properties, and multifunctionality. Here, we report a method that combines self-assembly and 3D printing to create ceramic architectures with hierarchical porosity spanning from the nano- to microscale. To programmably define their microscale porosity, an additive manufacturing method, known as direct ink writing, is used to create 3D lattices composed of cylindrical struts. Nanoscale porosity is generated within each strut by block copolymer templating followed by photopolymerization and pyrolysis in a non-oxidative environment, which transforms the preceramic polymer, polycarbosilane, into silicon oxycarbide with a "nanocoral" morphology. The resulting hierarchically porous ceramic lattices exhibit excellent mechanical energy absorption (0.31 MJ/m³), comparable to metal alloy foams. They also possess an order of magnitude lower thermal conductivity (0. 087–0.16 W/m·K) compared to bulk preceramic polymer-derived ceramics. Prior to pyrolysis, the printed architectures can be manipulated to produce more complex shapes, including lattices with twisted, helical, and overhang features as well as repeated folding to create an origami airplane. By combining self- and directed assembly, our approach opens new avenues for creating hierarchically porous ceramics.

Keywords: Additive manufacturing; Preceramic polymer; Porosity; Ceramic; Nanostructure; Lightweight; Insulator; Mechanical properties; Foams

¹ Materials and Manufacturing Directorate, Air Force Research Laboratory, Wright-Patterson AFB, OH 45433, United States

² UES, Inc., Dayton, OH 45432, United States

³ Department of Mechanical and Industrial Engineering, University of Massachusetts, Amherst, MA 01003-2210, United States

⁴ Department of Mechanical Engineering, Thomas J. Watson College of Engineering and Applied Science, State University of New York, Binghamton, NY 13902-6000, United States

⁵ Materials Science and Engineering Program, State University of New York, Binghamton, NY 13902-6000, United States

⁶ NRC Research Associateship Programs, The National Academies, Washington, DC 20001, United States

⁷ Harvard John A. Paulson School of Engineering and Applied Sciences, Harvard University, Cambridge, MA, United States

⁸ Wyss Institute for Biologically Inspired Engineering, Harvard University, Cambridge, MA, United States

^{*} Corresponding authors.

 $[\]textit{E-mail addresses:} \ Chen, W. \ (wenchen@umass.edu), \ Lewis, J.A. \ (jalewis@seas.harvard.edu), \ Dickerson, M.B. \ (matthew.dickerson.6@us.af.mil).$

Introduction

Hierarchically porous ceramics are of interest for myriad applications (e.g., lightweight architectures [1-10], catalyst supports [11], thermal insulation [12-14], photonics [15], and electrodes [16-18]) due to the ability to create such structures with tailored properties [2,15,19]. To date, both periodic and stochastic structures have been reported. For example, ultra-lightweight 3D octet trusses [20-24] and lattices [4,5,7,25] have recently been constructed that exhibit high specific stiffness and strength [6,20,26]. However, these nano-architected materials require expensive microfabrication methods [19,27,28] or two-photon lithography [25,29] to generate polymer templates that must then be coated via atomic layer deposition to transform them into the desired metal or ceramic structure. Hierarchically porous ceramics have also been fabricated on the macroscale via etching [30], pore formers/foaming agents [31,32], or freeze-drying [33], among others [34]. Although these methods create ceramics with lower densities and tailorable pore geometries, the pore sizes in these materials are generally 10s to 100s of microns in size, which does not produce the unique mechanical responses found in microfabricated structures [34].

Recently, additive manufacturing of preceramic polymers has been reported as an alternate route to creating architected ceramics [35,36]. By introducing photoactive groups along the polymer backbone, silicon carbide honeycombs were generated via stere-olithography [3,37] at larger scales, while corkscrews, gears, and microlattices were generated via two-photon lithography at smaller scales [38,39] for applications in aerospace or ballistic resistance. However, these architected ceramics lacked nanoscale features that would greatly enhance crack inhibition, toughness, and energy absorption.

Self-assembly of block copolymers offers an attractive alternative for generating nanostructured materials due to their processability, commercial availability, and ability to generate distinct morphologies by varying the composition, molecular weight, and relative ratio of each block [40-47]. Due to their amphiphilic nature, block copolymers undergo segregation to minimize the energetically unfavorable interactions between different blocks. Such interactions, which are determined by χN , where χ is the Flory-Huggins parameter and N is the degree of polymerization, can be controlled by varying the composition and molecular weight of each block, yielding a broad array of templating geometries [44-47]. Importantly, block copolymers are also well suited to templating preceramic polymers and thereby producing nanostructured ceramics [48-52] with tunable morphologies and properties by varying the preceramic-to-block copolymer ratio and composition. To date, most ceramics fabricated by this approach lack the 3D geometry needed for many targeted applications.

Here, we combine self-assembly and 3D printing of preceramic-block copolymer inks to create hierarchically porous ceramics. The self-assembling inks combine a preceramic polymer, polycarbosilane (PCS), with a triblock copolymer composed of poly(methyl methacrylate) (PMMA) and poly(*n*-butyl acrylate) (PnBA), which serve as ceramic and templating phases, respectively. The ink composition and rheology are tailored to enable direct writing of 3D lattices. Thiol–ene click chemistry is used

to react a thiol crosslinking agent with alkene groups on the PCS, allowing their self-assembled nanostructure to be "locked in" after printing and curing. The as-fabricated polymer lattices are mechanically robust and can be twisted, molded, or folded into more complex 3D shapes. The polymeric species are removed during pyrolysis resulting in 3D ceramic lattices composed of silicon oxycarbide (SiOC) and silicon carbide (SiC), which are temperature and corrosion resistant. Finally, we studied the pyrolyzed ceramic architectures to elucidate the effect of hierarchical porosity on their structure as well as mechanical and thermal properties.

Results

We created preceramic-block copolymer inks composed of PCS and PMMA-b-PnBA-b-PMMA for direct ink writing of 3D hierarchically porous lattices (Fig. 1). Both the PCS and the solvent (1butanol) selectively swell the hydrophobic PnBA segments within the block copolymer resulting in wormlike micelles [40,53] (Fig. 1a and b). To "lock in" this desired nanostructure in printed lattices (Fig. 1c), we incorporated a thiol crosslinker that reacts via thiol-ene click chemistry with the alkene side groups present on the preceramic polymer. The printed lattices are photocured upon exposure to UV light (Figs. 1d, S1). Importantly, this crosslinking step also hinders the migration of the preceramic polymer, which is a liquid at room temperature, to the surface of the printed filamentary features (Fig. S2). Finally, the printed and cured 3D lattices are transformed into the desired ceramic phase (SiOC) upon pyrolysis at 800 °C (Fig. 1e, Figs. S1, S3-S5).

The preceramic-block copolymer inks exhibited the requisite viscoelastic properties for direct ink writing of spanning filamentary features (Fig. 2). The inks possess a low-shear viscosity of 600 Pa·s at a shear stress of 1 Pa and exhibit shear thinning behavior, which facilitates their flow through fine nozzles during printing (Fig. 2a). In the linear elastic regime, the storage modulus ($G' \sim 3000$ Pa) exceeds the loss modulus (G''), indicating that the ink is a gel under quiescent conditions (Fig. 2b). The ink flows when its shear yield stress (\sim 32 Pa), as defined by the crossover point where G' = G''. Next, we assessed the ink printability as a function of both printing speed and applied pressure (Fig. 2c), where good printability is defined by the ability to print spanning filamentary features with a diameter approximately equivalent to the nozzle size. At high printing pressures and lower speeds, the diameter of the printed filaments greatly exceeds the nozzle size inhibiting the formation of 3D periodic lattices. Conversely, at lower printing pressures and high speeds, the printed filaments undergo considerable extensional flow leading to significant reductions in their diameter compared to the nozzle size. However, as delineated in Fig. 2C, a broad range of "good" printability conditions is attained when these two parameters are appropriately balanced.

Our self-assembling inks are well suited for printing 3D lattices composed of cylindrical filaments with controlled diameters (Fig. 3). The printed features are capable of spanning unsupported gaps without deformation [46–48] as well as maintaining their printed shape after pyrolysis (Fig. 3a and b, Fig. S6). The SiOC lattices exhibited a porous "nanocoral" morphology

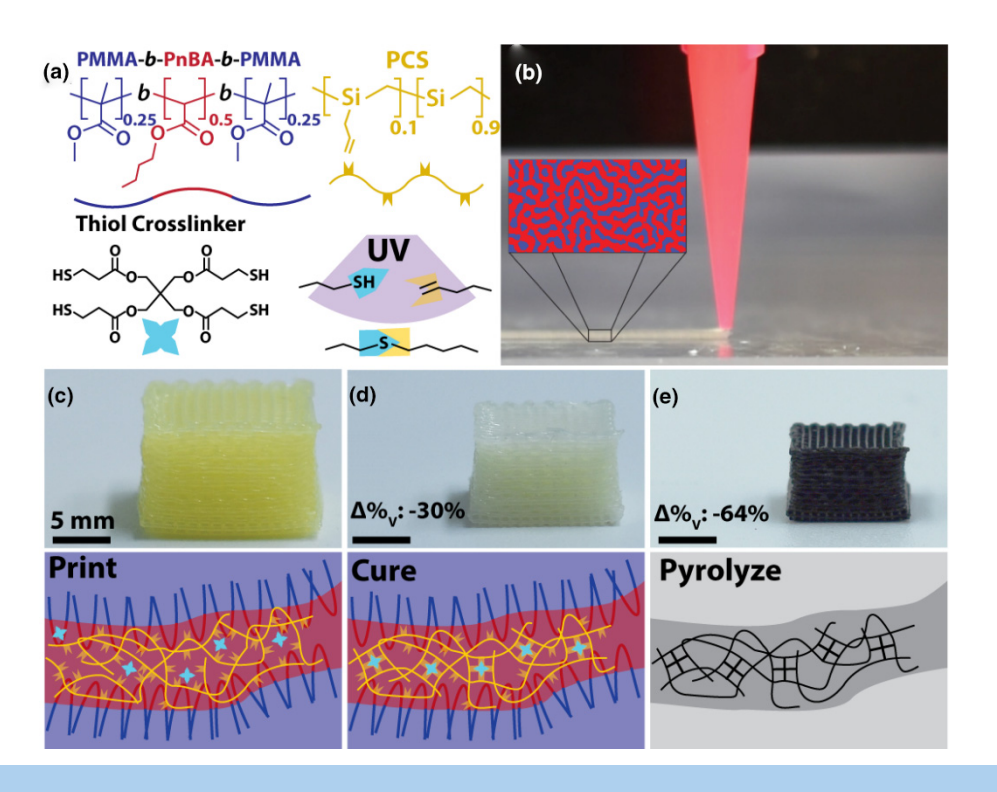


FIGURE 1

Preceramic-block copolymer composite inks. (a) Chemical composition of photopolymerizable, preceramic polymer/block copolymer ink that contains polycarbosilane (PCS), a triblock copolymer with poly(methyl methacrylate) (PMMA) and poly(n-butyl acrylate) (PnBA) blocks, and a thiol-based crosslinker. (b) Optical image of the preceramic-block copolymer ink during printing of a cylindrical feature [Inset depicts a schematic view of the wormlike morphology that arises due to self-assembly of the preceramic polymer/block copolymer ink], (c–e) optical images (top) of the as-printed, cured, and pyrolyzed 3D lattices fabricated by direct ink writing, respectively, and corresponding schematic views (bottom) depicting the arrangement of each ink constituent within a characteristic block copolymer domain. [Note: Characteristic volumetric shrinkage observed upon curing and pyrolysis are provided in dand e, respectively.].

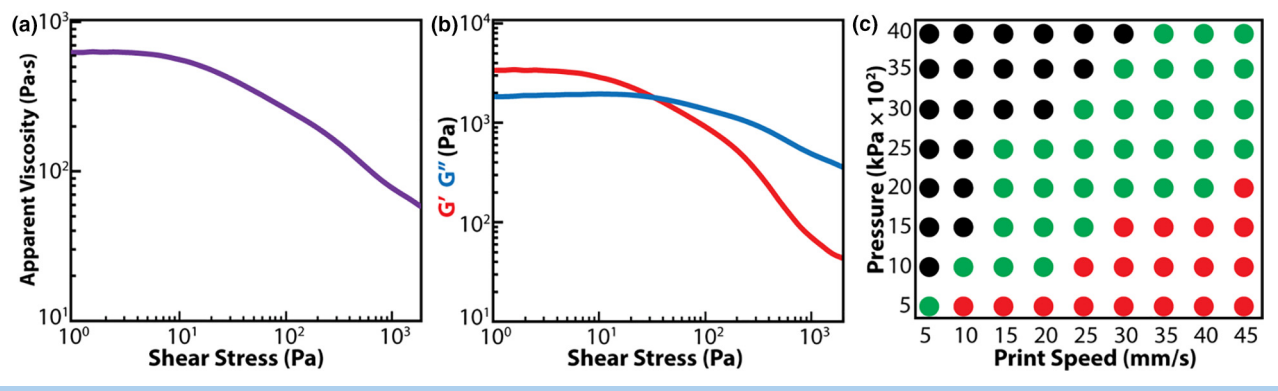


FIGURE 2

Ink rheology and printing behavior. (a) An amplitude sweep showing the storage (G') vs loss (G'') moduli. (b) Complex viscosity showing apparent viscosity vs oscillation stress. (c) Printing parameter map showing the available pressures and print speeds for our ink, where black dots indicate overextrusion, green indicate acceptable extrusion, and red indicate underextrusion.

(Fig. 3c), akin to our prior observations on thin films produced from similar materials (Fig. S7) [40,53]. Their nanoscale struts are more truncated compared to those observed in thin films, which were $\sim 1~\mu m$ thick [40,53]. This morphological difference is not unexpected, as their nanostructural evolution is strongly influenced by both surface and interfacial effects [54]. Importantly, these nanoscale features arise due to self-assembly within the preceramic-block copolymer ink, which leads to a wormlike morphology that persists during printing of inks with a PCP: BCP mass ratio of 2:3 (Fig. 3d). Since the preceramic polymer

preferentially swells the hydrophobic domains within the block copolymer, one can generate different morphologies by tailoring the PCP:BCP ratio [40], though this was outside the scope of this investigation.

Next, we investigated the mechanical behavior of these hierarchically porous ceramics (Fig. 4). A representative stress–strain curve of SiOC lattices ($\rho = 0.37 \text{ g/cm}^3$) tested under compression along the build (through-thickness) direction is shown in Fig. 4a (see also, Supplementary Movie 1). We note that bulk (i.e., non-porous) materials derived from SMP-10 polycarbosilane have a

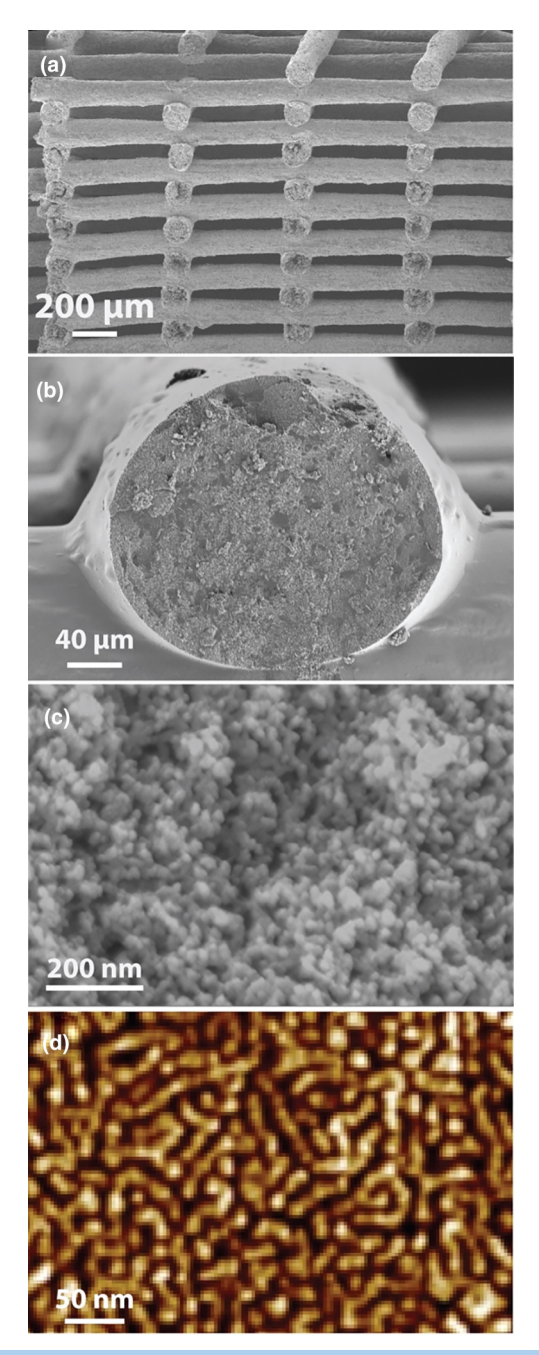


FIGURE 3

Direct writing of hierarchically porous ceramic lattices. (a) SEM image of printed 3D lattice (cross-sectional view), which shows that the printed struts are capable spanning unsupported regions with minimal deformation. (b) SEM image of representative printed strut (cross-sectional view) in the 3D lattice shown in (a), (c) SEM image of the pyrolyzed ink taken from a representative area of a strut (cross-section) shown in (b), and (d) AFM image of the preceramic polymer/block copolymer ink revealing its wormlike morphology, where PMMA (light) and PnBA/PCP (dark) are shown.

theoretical density of 2.15 g/cm³ [55] and pycnometry experiments performed on printed, pyrolyzed nanocoral woodpile lattices reveal that their density is 1.946 ± 0.002 g/cm³.

Unlike the typical catastrophic failure expected for brittle bulk ceramics under compressive loading conditions, the stress–strain response of these hierarchically porous lattices is analogous to

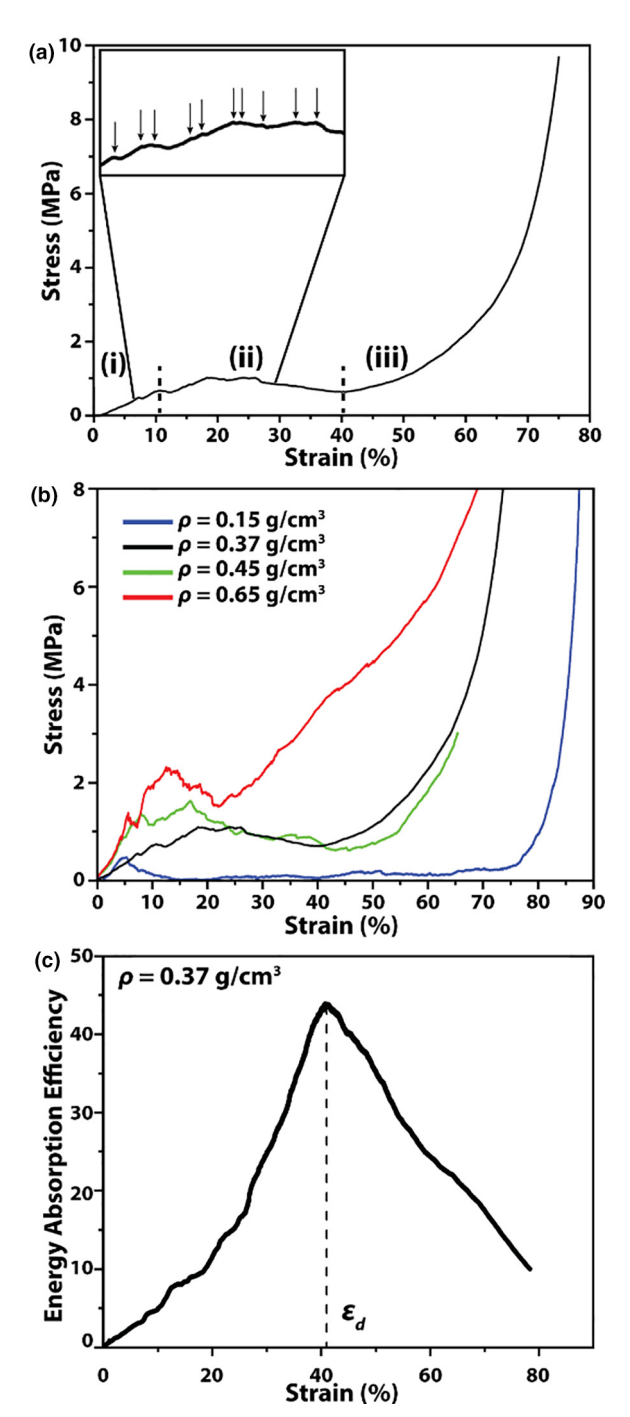


FIGURE 4

Mechanical properties of hierarchically porous ceramic lattices. (a) A representative compressive engineering stress–strain curve for a hierarchical porous ceramic lattice with a density of 0.37 g/cm³ and nanocoral SiOC struts. The graph shows regions of (i) linear elasticity, brittle crushing plateau, and (iii) final densification. Inset shows stress serrations within regions (i) and (ii) in greater detail, with arrows to guide the eye. (b) Compressive stress–strain curves for hierarchical porous ceramic lattices with different densities and nanocoral SiOC struts. (c) Energy absorption efficiency plot of a lattice with a density of 0.37 g/cm³ showing how the densification onset strain, ε_{dr} is identified using the energy absorption efficiency method.

that of many stochastic ceramic foams[56], characterized by three progressive deformation regimes (Fig. 4a): (i) linear elastic, (ii) brittle crushing plateau, and (iii) final densification. Several stress serrations associated with subtle stress drops are also visible in the elastic regime (Fig. 4a inset), which may stem from localized cracking of weaker regions within these architectures. Nevertheless, these architectures exhibit a progressive crushing plateau behavior at the macroscale until final densification, which is denoted by the rapid rise after the plateau. These results are not unexpected, given that our nanocoral morphology is similar to stochastic foam architectures that also exhibit progressive crushing under loading.[57,58].

We then expanded these measurements to architected lattices with different center-to-center separation distances between adjacent filaments with densities of $\rho = 0.15, 0.37, 0.45,$ and 0.65 g/cm³ (Figs. 4b and S8). Note, the as-pyrolyzed bulk nanocoral SiOC, i.e., no spacing between adjacent filaments, has a density of 0.65 g/cm³. Given that the theoretical density of bulk SiOC [55] (i.e., non-porous, polymer-derived) is $\rho_s = 2.15$ g/ cm³, these architected lattices have relative densities of ρ / ρ_s = 0.07, 0.17, 0.21, and 0.30, respectively. Their yield strength, σ_{y} , defined as peak stress before the onset of the plateau regime, scales linearly with ρ/ρ_s . Notably, σ_v increases from approximately 0.48 MPa at ρ/ρ_s = 0.07 to 1.62 MPa at ρ/ρ_s = 0.30, with the bulk nanocoral SiOC architectures exhibiting the highest yield strength of $\sigma_v \approx 2.31$ MPa. Moreover, we found that our hierarchical nanocoral ceramics fail gradually, akin to stochastic ceramic foams [56], due to a progressive crushing response. This behavior may arise from both their constituent material (nanoscale ceramic) and structural topology (hierarchical nanocoral architecture). Nanoscale size effects on the brittle-to-ductile transition of ceramic materials has been reported when their characteristic feature size is below ~ 100 nm [6,59]. Nanoscale ceramics exhibit both near theoretical strength and large ductility [20], in striking contrast to the catastrophic premature failure of bulk ceramic materials. Mechanistically, when the characteristic feature size is less than the intrinsic plastic zone size, defects (especially surface defects) will not propagate into micro- or macroscale cracks, which gives rise to the high ductility observed in nanoscale ceramics [60]. In addition, the loading orientation also plays a critical role in mechanical behavior of architected materials. The deformation mode of our HPC lattices along the through-thickness direction resembles that of many periodic honeycombs or lattices loaded out-of-plane, which results in a more confined stress state to facilitate progressive deformation [61]. Such stable deformation behavior is desirable for energy absorption applications and is fundamentally distinct from the in-plane deformation behavior of periodic honeycombs or lattice structures, in which strain often localizes into narrow shear bands due to collective buckling or collapse of cell walls that result in dramatic stress "valleys" [62] rather than a series of minor stress serrations, such as in our HPCs.

The compressive yield strength and energy absorption as a function of the relative density of these architected SiOC lattices is shown in Fig. 5 (and versus density in Fig. S9). For comparison, recent data reported for other ceramic architectures, including periodic SiOC and Al_2O_3 octet trusses [6,20,26,63], SiC, SiOC, and Al_2O_3 foams [65–68], and SiCN micro-lattices [35] are also shown. At similar relative densities, the yield strengths of our hierarchical porous ceramics (HPCs) are comparable to many stochastic ceramic foams, but lower than the values reported

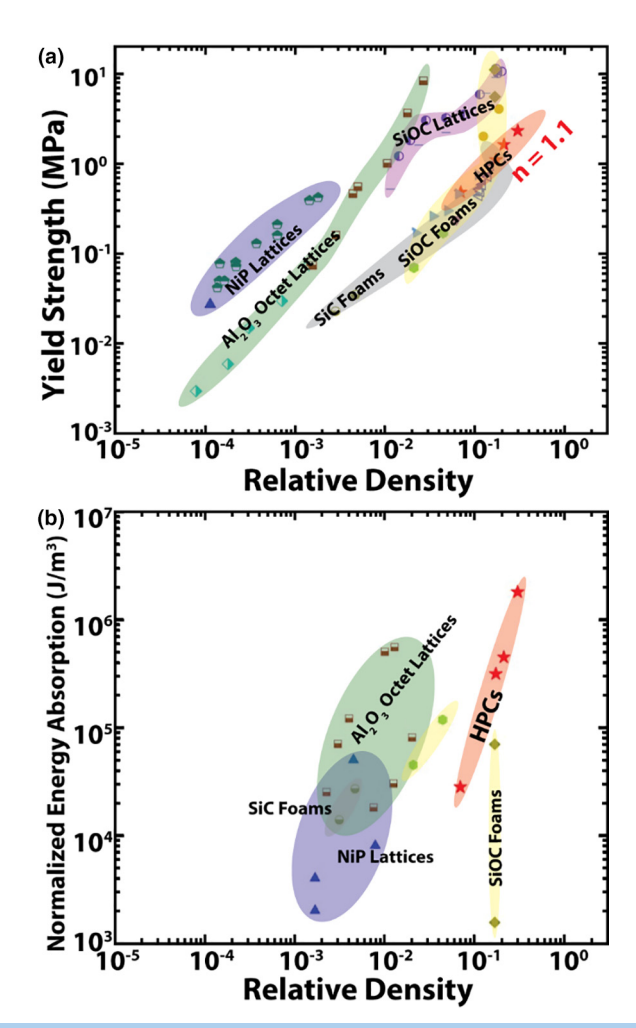


FIGURE 5

Ashby plots comparing the mechanical performance of our hierarchical porous ceramic (HPCs) lattices to other architected materials [6,20,35,56,63-68]. (a) normalized energy absorption and (b) yield strength as a function of relative density. [Note: Our data is shown in the red region as red stars.].

for octet trusses, which exhibit exceptional stiffnesses and strengths (Fig. 5a). The yield strength of an open-cell architected material scales with relative density, as given by [56]:

$$\frac{\sigma}{\sigma_s} \propto \left(\frac{\rho}{\rho_s}\right)^n \tag{1}$$

where σ_s and ρ_s are the yield strength and density of the bulk SiOC, respectively, and σ and ρ are the yield strength and density of the hierarchical porous ceramics, respectively. The scaling exponent, n, reflects the nature of the deformation mode in the architected material: $n \approx 1$ suggests stretch-dominated deformation, while $n \approx 2 \sim 3$ is indicative of bend-dominated deformation [69]. For our HPCs, we found that $n \approx 1.1$, suggesting that they exhibit stretch-dominated deformation.

The energy absorption behavior of these materials is also crucial for applications such as load-bearing or blast protection, which can be maximized by a high stress plateau over a prolonged plastic regime. The progressive plateau behavior with much smaller stress drops/serrations exhibited by these hierarchically porous ceramics gives rise to a substantially higher energy absorption compared to their stochastic foam counter-

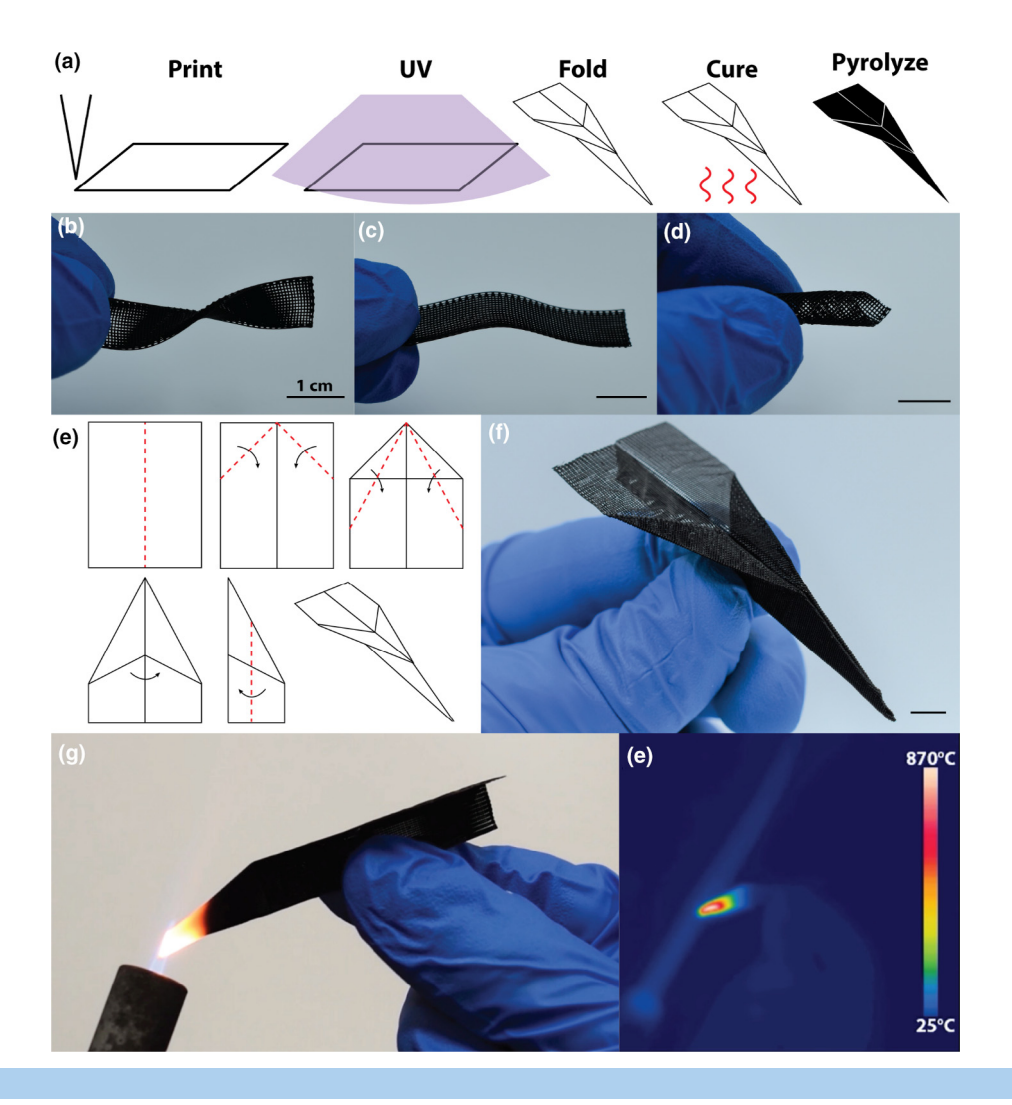


FIGURE 6

Twisted, rolled, and folded hierarchically porous ceramic architectures. (a) Schematic illustration showing how printed lattices are folded into complex objects. (b–d) Images of printed lattices that are twisted and rolled into 3D structures and (e and f) Schematic illustration of the folding sequence used and corresponding image of printed lattice folded into a "paper" airplane, respectively. (g and h) Optical and thermal images of resulting SiOC airplane being heated in a butane flame obtained using visible and IR cameras, respectively. Scale bars = 1 cm.

parts (Fig. 5b). The energy absorption per unit volume, W, is measured by the integral of the stress-strain curve up to the densification onset strain, ε_d , which can be quantitatively determined by the energy-absorption-efficiency method [70,71]. In this method, an energy absorption efficiency parameter, $\eta(\varepsilon)=rac{\int_0^\varepsilon\sigma(\varepsilon)d\varepsilon}{\sigma(\varepsilon)}$, is used and ε_d is derived by locating the global maximum of efficiency $\eta(\varepsilon)$ with increasing strain ε , i.e., $\frac{d\eta(\varepsilon)}{d\varepsilon}|_{\varepsilon=\varepsilon}=0$. A typical η – ε curve is shown in the Fig. 4c where ε_d is denoted. The energy absorption up to densification strain, $W = \int_0^{\varepsilon_d} \sigma(\varepsilon) d\varepsilon$ was calculated for our architected lattices and plotted alongside other recently reported values as illustrated in Fig. 5b [6,20,26,35,63-68]. W continuously increases from 0.028 to 0.45 MJ/m³ as the relative density of the HPCs increases from 0.07 to 0.21. The bulk nanocoral SiOC shows further enhanced energy absorption. This trend is consistent with the strong dependence of the yield strength and plateau stress on their relative density (Fig. 5a). As one example, when $\rho/\rho_s \approx 0.15$, $W = 0.31 \text{ MJ/m}^3$ for our architected lattices, which is nearly five times greater than that of $\sim 0.065 \text{ MJ/m}^3$ for conventional SiOC

foams [66]. While nanoscale octet trusses exhibit comparable energy absorption at even lower relative density, their exquisite fabrication method requires a combination of two-photon lithography followed by atomic layer deposition that is both costly and difficult to scale up.

Interestingly, these lattices could be easily molded, rolled, and folded after printing and UV curing (Fig. 6). As a simple demonstration, we created a twisted "bowtie" shape (Fig. 6b) that possesses negative curvature, a "wave" that possesses positive curvature (Fig. 6c), and a cylinder (Fig. 6d) from these architected lattices. As a final demonstration, we created a "paper airplane" via a multi-step folding process (Fig. 6e, f). In each case, the final geometry is retained during pyrolysis without warping or shape distortions. Importantly, these lattice-based architectures could be easily handled even when they were exposed to flame over short (~cm scale) distances (Movies S2). In fact, when the ceramic "airplane" was exposed to a butane torch, IR imaging revealed localized temperatures of up to 870 °C at the nose of the plane, while the temperature barely rose above room temperature at the end of the airplane where it was being held manually

(Movie S3). This demonstration suggests that these hierarchically porous ceramic lattices would be well suited for high temperature insulation applications [72]. Though the large surface area arising from their nanocoral architecture enhances their susceptibility to oxidation at high temperatures, these materials may find potential application as cladding or in an internal layer not readily exposed to air.

Bulk SiOC derived from pure preceramic polymers typically exhibits a low intrinsic thermal conductivity (k) ranging from 1.5-2.4 W/m·K [72,73] due in part to their glassy matrices as well as residual hydrogen and dangling bonds that scatter phonons. By contrast, our architected ceramic lattices exhibit thermal conductivity values between 0.087–0.16 W/m·K (Fig. S10, Table S1), an order of magnitude lower than bulk SiOC and within an order of magnitude of macroporous SiOC materials [74]. However, their thermal conductivity as a function of density did not follow the expected scaling behavior of $k \propto \rho^{1.5}$. We observed significant scatter in the measured data, which may arise due to compositional variations (relative amount of SiC, graphite, and SiO₂ phases) between lattices, which has also been observed for bulk SiOC [75]. Looking ahead, we will focus our efforts on further understanding and optimizing their composition and thermal properties.

Conclusion

We have developed a method for fabricating macroscale ceramic architectures with hierarchical porosity that spans from the nano- to microscale. These architected ceramics were created through a combination of self-assembly and printing, with more complex geometries achieved by subsequently twisting and folding printed lattices prior to curing and pyrolyzing. These hierarchically porous ceramic architectures displayed both high specific strength and mechanical energy absorption, which are of interest for aerospace and structural applications. They also exhibited thermal conductivities that were an order of magnitude lower than bulk SiOC derived from preceramic polymers. This nascent strategy of 3D printing in combination with self-assembly opens new avenues to fabricating architected matter for myriad functional, structural, and biological applications.

Methods

Materials

A preceramic polymer (PCP) composed of polycarbosilane, (StarPCS SMP-10, Starfire Systems, Schenectady, NY) with a molecular weight, M_w , of 7500 g/mol, and a polydispersity index (PDI) of 8.60 was stored at -20 °C and used without further modification. A block copolymer (BCP) composed of poly(methyl methacrylate) (PMMA) and poly(n-butyl acrylate) (PnBA) with 25 wt% PMMA-b-50 wt% PnBA-b-25 wt% PMMA, total M_w of 64,000 g/mol and PDI of 1.1912 (Kurarity LA4285, Kurary, Japan) was dried and stored at 80 °C, as recommended by the manufacturer. 1-Butanol (Sigma-Aldrich, Burlington, MA) was used as a midblock selective solvent. Pentaerythritol mercaptopropionate) (Sigma-Aldrich, CAS#7575-23-7) was used as a thiol crosslinker and phenylbis(2,4,6-trimethylbenzoyl) phosphine oxide (Sigma-Aldrich CAS#511447) was used as a photoinitiator.

Preceramic-block copolymer inks

The inks were prepared by mixing 1.8 g of BCP to 2 g of 1-butanol in a 25 mL glass vial with a stir bar and heated in an aluminum bead bath to 80 °C while stirring. Once BCP has fully dissolved (\sim 60 min), 0.05 g of photoinitiator, 0.15 g of thiol crosslinker, and 1.2 g of room temperature SMP-10 were added to the vial, heated to 80 °C while stirring to fully dissolve (\sim 10 min). After all components were fully mixed, the vial was removed from heat and allowed to cool to room temperature. Inks were prepared immediately before printing and not allowed to sit for more than four hours. Inks not immediately used were stored away from light to prevent crosslinking.

Before printing, 1 g of acetone was added to an ink vial and the contents mixed in an orbital planetary mixer (Thinky, Laguna Hills, CA) for 12 min at 2000 RPM.

Ink rheology

Stress viscometry and oscillatory measurements were carried out on the preceramic-block copolymer inks using a hybrid rheometer (Discovery HR-3 TA Instruments, New Castle, DE) equipped with a 40 mm parallel plate geometry. Stress viscometry measurements were carried out by subjecting the inks by ramping the applied shear stress from 0.01 to 1000 Pa. Stress sweeps were carried out between 1– and 2000 Pa at frequency of 1 Hz.

Direct ink writing

Each ink was poured into a 3 mL syringe (Nordson, Westlake, OH). Samples were printed using an Aerotech (Aerotech, Pittsburgh, PA) gantry printer. Pressure was controlled using an EFD Ultimus V (Nordson, Westlake, OH) pressure regulator. 3D lattices were printed at a pressure of 350 psi with a print speed of 20 mm/s onto a glass substrate (Fisher Scientific, Waltham, MA) using 250 μm smoothflow tapered tip nozzles (Nordson) unless otherwise noted.

After printing, parts were placed in a vacuum desiccator and dried for 15 min to remove solvent (0.1 MPa). Parts were removed from the desiccator and placed in a UV curing chamber (Model DR-301C, Asiga, Australia) for 30 min to UV crosslink. Samples were thermally cured (to further crosslink the polycarbosilane) in a vacuum oven where they were heated at 1 $^{\circ}\text{C/min}$ and held at 160 and 230 $^{\circ}\text{C}$ for 1 h each. Crosslinking of the preceramic polymer is indicated by a color change from yellow to white/ivory. Additionally, cured parts are noticeably stiffer than uncured parts. Pyrolysis was carried out up to 800 $^{\circ}\text{C}$ (1 h hold) in flowing argon gas in an alumina tube furnace equipped with a graphite sleeve at a heating rate of 1 $^{\circ}\text{C/min}$.

Pycnometry

Pyconmetry was performed on a Micrometrics (Norcross, GA) AccuPyc1330 using He gas. Samples were dried in a vacuum hood for 48 h prior to measuring their mass and volume. Five volume measurements were acquired and their average values and standard deviations are reported.

Mechanical properties

Uniaxial compression tests (Instron 5969, Norwood, MA) were performed on 3D ceramic lattices (5 mm in length and width and 4 mm in height) with a center-to-center filament spacing

ranging from 250 μm to 1 mm. Their relative densities varied from ${\sim}0.2$ to 1 when normalized by bulk density of the nanocoral SiOC (i.e., no gap between adjacent filaments) or 0.07–0.30 when normalized by the theoretical density of SiOC (see Fig. S9). The strain was measured by a non-contact AVE2 video extensometer (Instron, Norwood, MA) under a quasi-static strain rate of 2 \times 10 $^{-4}$ s $^{-1}$. A digital camera (Canon EOS 6D) was employed to capture the real-time deformation morphology of these ceramic architectures. Three samples were tested for each condition.

Microstructural characterization

Atomic force microscopy (AFM, Bruker Dimension 3100, Billerica, MA) was carried out on dried thin films and filaments composed of the PCP-BCP ink in standard tapping mode using Nanosensor tips (PPP-NCHR, Neuchâtel, Switzerland). The cantilever resonance frequency was roughly 330 kHz. Scanning electron microscopy (SEM) of pyrolyzed ceramic films was performed on a Zeiss Gemini 500 field emission SEM operated at 0.5 keV (Carl Zeiss AG, Oberochen, Germany). Films were sputter coated with $\sim\!10$ nm Ir before imaging. Transmission electron microscopy (TEM) images were taken in an FEI Talos operating in STEM mode with all samples sputter coated with $\sim\!10$ nm of iridium.

X-ray diffraction

Sample was ground with a mortar and pestle using ethanol as a lubricant and the paste was dried over 48 h at 120 °C. The powder was placed into a zero background Si holder in a Bruker D2 Phaser benchtop (Billerica, Massachusetts) XRD operated at 30 kV and 10 mA with a Cu K α tube. The sample was scanned from 10 to 90 degrees (2 θ) with a step size of 0.02 degrees with 0.5 s per step for a total collection time of 2100 s.

Thermal properties

The specific heat of each sample was measured using the modulated digital scanning calorimetry technique (TA Instruments Q200). Their thermal diffusivities were measured using the flash diffusivity technique (Anter Flashline 2000), each sample being exposed six times. The transient temperature response of the sample was fit to the Clark and Taylor model [74,76] with the thermal diffusivity as a free parameter. Each sample is optically dense, so radiation heat transfer is considered negligible near room temperature.

CRediT authorship contribution statement

John J. Bowen: Conceptualization, Investigation, Methodology, Writing – original draft, Writing – review & editing. Shahryar Mooraj: Conceptualization, Investigation, Methodology, Writing – original draft, Writing – review & editing. Jacob A. Goodman: Investigation, Writing – original draft, Writing – review & editing. Siyuan Peng: Investigation, Methodology, Writing – original draft, Writing – review & editing. Dayton P. Street: Methodology, Writing – original draft, Writing – review & editing. Benito Roman-Manso: Investigation, Methodology, Writing – original draft, Writing – review & editing. Emily C. Davidson: Methodology, Writing – original draft, Writing – review & editing. Kara L. Martin: Methodology

ogy, Writing – original draft, Writing – review & editing. **Lisa M. Rueschhoff:** Methodology, Writing – original draft, Writing – review & editing. **Scott N. Schiffres:** Formal analysis, Writing – original draft, Writing – review & editing, Supervision. **Wen Chen:** Conceptualization, Formal analysis, Writing – original draft, Writing – review & editing, Supervision, Project administration, Funding acquisition. **Jennifer A. Lewis:** Writing – original draft, Writing – review & editing, Supervision, Project administration, Funding acquisition. **Matthew B. Dickerson:** Conceptualization, Writing – original draft, Writing – review & editing, Supervision, Project administration, Funding acquisition.

Declaration of Competing Interest

The authors declare that they have no known competing financial interests or personal relationships that could have appeared to influence the work reported in this paper.

Acknowledgements

MBD and JJB acknowledge support from the OUSD (R&E) Laboratory University Collaborative Initiative (LUCI) Fellowship Program. JJB acknowledges John Drazin for help in XRD measurements and analysis. MBD and LMR acknowledge core funding from AFRL/RX. KLM supported by AFRL/AFOSR under the Aerospace Composites Portfolio (PO: Dr. Ming-Jen Pan). DPS was supported by a Research Associate Program Fellowship Award from the National Research Council. WC acknowledges support from the National Science Foundation (DMR 2134715) and UMass Amherst Faculty Start-up fund. BRM, ED, and JAL gratefully acknowledge support from the Office of Naval Research Vannevar Bush Faculty Fellowship program (N000141612823) and the National Science Foundation through the Harvard MRSEC (DMR-2011754).

Appendix A. Supplementary data

Supplementary data to this article can be found online at https://doi.org/10.1016/j.mattod.2022.07.002.

References

- [1] J.T. Muth et al., PNAS 114 (8) (2017) 1832.
- [2] J. Bauer et al., Adv. Mater. 29 (40) (2017) 1701850.
- [3] T.A. Schaedler, W.B. Carter, Annu. Rev. Mater. Res. 46 (1) (2016) 187.
- [4] N.G. Dou et al., Nano Lett. 18 (8) (2018) 4755.
- [5] A.J. Mateos et al., Adv. Funct. Mater. 29 (5) (2019) 1806772.
- [6] L.R. Meza, S. Das, J.R. Greer, Science 345 (6202) (2014) 1322.
- [7] X. Zhang et al., PNAS 116 (14) (2019) 6665.
- [8] B. Román-Manso et al., J. Eur. Ceram. Soc. 38 (5) (2018) 2265.
- [9] X. Zheng et al., Science 344 (6190) (2014) 1373.
- [10] B. Román-Manso et al., ACS Appl. Mater. Interfaces 13 (7) (2021) 8976.
- [11] C. Zhu, et al., Sci. Adv. (2018) 4 (8), eaas9459.
- [12] J. Liu et al., Ceramics 46 (6) (2020) 7149.
- [13] X. Zhang et al., J. Eur. Ceram. Soc. 40 (3) (2020) 930.
- [14] H. Wang et al., Sci. Adv. 3 (6) (2017) e1603170.
- [15] X. Wen et al., Nat. Mater. 20 (11) (2021) 1506.
- [16] C. Kim et al., ACS Nano 12 (12) (2018) 11838.
- [17] K. Sun et al., Adv. Mater. 25 (33) (2013) 4539.
- [18] T.-S. Wei et al., Adv. Mater. 30 (16) (2018) 1703027.
- [19] A. Guell Izard et al., Small 15 (45) (2019) 1903834.
- [20] L.R. Meza et al., PNAS 112 (37) (2015) 11502.
- [21] C. Gunderson et al., Adv. Eng. Mater. 23 (5) (2021) 2001293.
- [22] C. Ling et al., Mater. Des. 162 (2019) 106.
- [23] J.U. Surjadi, et al.., iScience (2021) 24 (7), 102789.

- [24] J.U. Surjadi et al., NPG Asia Mater. 13 (1) (2021) 36.
- [25] A. Vyatskikh et al., Nat. Commun. 9 (1) (2018) 593.
- [26] L.R. Meza, J.R. Greer, J. Mater. Sci. 49 (6) (2014) 2496.
- [27] C.M. Portela et al., PNAS 117 (11) (2020) 5686.
- [28] M.-T. Hsieh et al., J. Mech. Phys. Solids 125 (2019) 401.
- [29] J. Schmidt et al., Addit. Manuf. 30 (2019) 100913.
- [30] D. Liu et al., Chem. Eng. J. 397 (2020) 125392.
- [31] C. Minas et al., Adv. Mater. 28 (45) (2016) 9993.
- [32] L. Alison et al., Sci. Rep. 9 (1) (2019) 409.
- [33] N. Arai, K.T. Faber, Scr. Mater. 162 (2019) 72.
- [34] A. Lichtner et al., J. Am. Ceram. Soc. 99 (3) (2016) 979.
- [35] Z.C. Eckel et al., Science 351 (6268) (2016) 58.
- [36] G. Liu, et al., Sci. Adv. (2018) 4 (8), eaat0641.
- [37] J.M. Hundley et al., Addit. Manuf. 18 (2017) 95.
- [38] N.R. Brodnik et al., Addit. Manuf. 31 (2020) 100957.
- [39] H. Cui et al., J. Mater. Res. 33 (3) (2018) 360.
- [40] J.J. Bowen et al., Macromolecules 53 (17) (2020) 7528.
- [41] M.E. Seitz et al., Macromolecules 40 (4) (2007) 1218.
- [42] H. Kishi et al., Express Polym, Lett. 11 (2017) 765.
- [43] P.L. Drzal, K.R. Shull, Macromolecules 36 (6) (2003) 2000.
- [44] F.S. Bates, Science 251 (4996) (1991) 898.
- [45] F.S. Bates, G.H. Fredrickson, Annu. Rev. Phys. Chem. 41 (1990) 525.
- [46] F.S. Bates, G.H. Fredrickson, Phys. Today 52 (2) (1999) 32.
- [47] M.W. Matsen, F.S. Bates, Macromolecules 29 (23) (1996) 7641.
- [48] J. Wan et al., Chem. Mater. 17 (23) (2005) 5613.
- [49] M. Kamperman et al., Nano Lett. 9 (7) (2009) 2756.
- [50] M.C. Orilall, U. Wiesner, Chem. Soc. Rev. 40 (2) (2011) 520.
- [51] E.M. Susca et al., Chem. Mater. 28 (7) (2016) 2131.

- [52] E.M. Susca et al., Adv. Func. Mater. 31 (40) (2019) 1902565.
- [53] L.M. Rueschhoff et al., ACS Appl. Nano Mater. 2 (1) (2019) 250.
- [54] J.N.L. Albert, T.H. Epps, Mater. Today 13 (6) (2010) 24.
- [55] T.S. Key et al., J. Euro. Ceram. Soc. 41 (13) (2021) 6356.
- [56] M.F. Ashby, L.J. Gibson, PSUC Cambridge, UK, (1997) 175.
- [57] A.M. Parvanian et al., J Am. Ceram. Soc. 102 (4) (2019) 2009.
- [58] S.K. Maiti, L.J. Gibson, M.F. Ashby, Acta Metall. 32 (11) (1984) 1963.
- [60] T.L. Anderson, Fracture Mechanics: Fundamentals and Applications, CRC Press,
- [61] K. Huang et al., J. Euro. Ceram. Soc. 41 (15) (2021) 7552.
- [62] M.-S. Pham et al., Nature 565 (7739) (2019) 305.

[59] D. Jang et al., Nat. Mater. 12 (10) (2013) 893.

- [63] X. Zheng et al., Nat. Mater. 15 (10) (2016) 1100.
- [64] T.A. Schaedler et al., Science 334 (6058) (2011) 962.
- [65] P. Wilson, S. Vijayan, K. Prabhakaran, Int. J. Appl. Ceram. Technol. 17 (2) (2020) 519
- [66] P. Colombo et al., Adv. Eng. Mater. 5 (11) (2003) 802.
- [67] A. Choudhary et al., Adv. Eng. Mater. 20 (3) (2018) 1700586.
- [68] D.C. Jana, G. Sundararajan, K. Chattopadhyay, J. Am. Ceram. Soc. 100 (1) (2017) 312.
 - [69] w. Chen, et al.., Sci. Adv. (2019) 5 (9), eaaw1937.
- [70] S. Peng et al., Scripta Mater. 190 (2021) 46.
- [71] W. Chen et al., Acta Mater. 73 (2014) 259.
- [72] A. Gurlo et al., J. Am. Ceram. Soc. 99 (1) (2016) 281.
- [73] C. Stabler et al., Mater. 11 (2) (2018) 279.
- [74] L. Qiu et al., Int. J. Thermophys. 35 (1) (2014) 76.
- [75] C. Stabler et al., J. Am. Ceram. Soc. 101 (11) (2018) 4817.
- [76] L.M. Clark Iii, R.E. Taylor, J. Appl. Phys. 46 (2) (1975) 714.